

1 **Marine Boundary Layer Structure as Observed by A-train**
2 **Satellites**

3
4

5 **Tao Luo, Zhien Wang, Damao Zhang and Bing Chen**

6 University of Wyoming, Dept. Atmospheric Science, Laramie, WY, USA

7 Correspondence to: Z. Wang (zwang@uwyo.edu)

8

9 **Abstract**

10 The marine boundary layer (MBL) structure is important to the marine low cloud processes,
11 and the exchange of heat, momentum, and moisture between oceans and the low atmosphere.
12 This study examines the MBL structure over the eastern Pacific region and further explores
13 the controlling factors of MBL structure over the global oceans with a new 4-year satellite-
14 based dataset. The MBL top (BLH) and the mixing layer height (MLH) were identified using
15 the MBL aerosol lidar backscattering from the CALIPSO (Cloud-Aerosol Lidar and Infrared
16 Pathfinder Satellite Observations). Results showed that the MBL is generally decoupled with
17 MLH/BLH ratio ranging from ~ 0.5 to ~ 0.8 . The MBL decoupling magnitude is mainly
18 controlled by estimated inversion strength (EIS), which in turn controls the cloud top
19 entrainment process. The systematic differences between drizzling and non-drizzling
20 stratocumulus tops also show dependence on EIS. This may be related to the meso-scale
21 circulations or gravity wave in the MBL. Further analysis indicates that the MBL shows a
22 similar decoupled structure for clear sky and cumulus cloud-topped conditions, but is better
23 mixed under stratiform cloud breakup and overcast conditions.

24 **1 Introduction**

25 The planetary boundary layer is the lowest part of the troposphere that is directly influenced
26 by the Earth's surface. It is considered to be important for the exchange of heat, momentum,
27 and moisture between the surface and the upper troposphere (Stull, 1988). Over oceans, the
28 marine boundary layer (MBL) clouds are frequently present within the MBL, making

1 significant contributions to the energy and moisture budgets of the earth because of their high
2 albedo (Klein and Hartmann, 1993; Norris and Leovy, 1994; Norris, 1998; Wood and
3 Bretherton, 2004). Despite decades of research efforts, the MBL clouds are still one of the
4 primary contributors to the uncertainty in the model predictions of climate change (Bony and
5 Dufresne, 2005; Randall et al., 2007; Wyant et al., 2015). Because of the close interactions of
6 MBL clouds with the vertical structure and turbulence of the MBL, the representation of
7 convection and MBL processes is critical to the successful climate simulations (Randall et al.
8 1985; Albrecht et al., 1995; Bony and Dufresne, 2005; Wyant et al., 2010; Zhang, et al.,
9 2011).

10 The decoupling of the MBL is frequently observed at the downwind of the subtropical
11 stratocumulus regions when the turbulence does not strong enough to maintain a well-mixed
12 MBL, especially when the MBL is higher than 1km (Bretherton and Wyant, 1997; Wood and
13 Bretherton, 2004; Jone et al., 2011; Caldwell et al., 2012). A wide range of factors controls
14 the MBL decoupling. Bretherton and Wyant (1997) suggested that the decoupling structure is
15 mainly driven by an increasing ratio of the surface latent heat flux to the net radiative cooling
16 in the cloud and that other factors such as drizzle, the vertical distribution of radiative cooling
17 in the cloud, and sensible heat fluxes, only play less important roles. Meanwhile, Zhou et al.
18 (2015) showed that the entrainment of the dry warm air above the inversion could be the
19 dominant factor triggering the systematic decoupling, while surface latent heat flux,
20 precipitation, and diurnal circulation did not play major roles.

21 The MBL structure and processes are still not well understood with observations mainly
22 limited to specific case studies in early studies (Wood and Bretherton, 2004). The boundary
23 layer structure can be derived from ground-based observations such as sounding (Seidel et al.,
24 2010) or lidar (Emeis et al. 2008). However, ground-based observations of the MBL over the
25 global oceans are sparse and may be not representative. Wood and Bretherton (2004) were the
26 first to attempt a combination of MODIS and reanalysis data to study the MBL decoupling,
27 though this passive remote sensing cannot produce direct measurements of MBL structures.

28 New satellite-based observations allow innovative ways to observe the boundary layer
29 structure. The global boundary layer height (BLH) climatology has been derived by using
30 Global Positioning System radio occultation (GPS-RO) measurements (Ratnam and Basha,
31 2010; Guo et al, 2011; Ao et al, 2012), the Lidar In-space Technology Experiment (LITE)
32 (Randall et al., 1998), the Geoscience Laser Altimeter System (GLAS) (Palm et al., 2005),

1 and the Cloud-Aerosol Lidar with Orthogonal Polarization (CALIOP) (Jordan et al., 2010,
2 McGrath-Spangler and Denning, 2012, 2013). GPS-RO provides a valuable global view of
3 height-resolved refractivity or moisture structure of boundary layer, but suffers with very
4 coarse spatial resolutions (200 m in vertical and ~200 km horizontal) and has limited
5 penetration into the lowest 500 m of the atmosphere (Xie et al, 2012). Satellite-based lidar is
6 sensitive to boundary layer aerosols and clouds, providing global measurements of aerosol
7 properties and their vertical distributions. As the aerosol vertical distribution in the boundary
8 layer is heavily influenced by the boundary layer thermal structure, aerosol structures were
9 used as a good proxy to study the MBL structures (Stull and Eloranta, 1984; Boers et al.,
10 1984; Melfi et al., 1985; Boers and Eloranta, 1986; Leventidou et al., 2013; Luo, et al., 2014a;
11 Kong and Fan, 2015).

12 Early studies have shown that satellite-based lidar is effective at deriving global BLH
13 distributions (Randall et al., 1998; Palm et al., 2005; Jordan et al., 2010; McGrath-Spangler
14 and Denning, 2012, 2013). This is especially true when using CALIOP observations, because
15 of their much finer vertical (30m) and horizontal resolution (333m) in the lower troposphere.
16 The aforementioned studies used gradient or variance methods over land and ocean under all-
17 sky or no-optically-thick-cloud conditions. Over land, the gradient or variance methods could
18 identify the BLH, which is usually lower than the aerosol layer (Luo et al., 2014a). However,
19 over oceans, the BLH is associated with the aerosol layer top (clear sky) or stratiform cloud
20 top (cloudy sky). Under decoupled MBL conditions, a well-mixed layer usually exists below
21 the BLH with a stronger gradient in aerosol loading near the mixed layer height (MLH) than
22 near the BLH (Luo, et al., 2014a). Thus, the aforementioned studies have the potential to
23 report MLH as BLH as they did not fully consider the MBL decoupled structure in choosing
24 lidar methodologies. In the MBL, difficulties in differentiating between the stratiform clouds
25 and cumulus clouds could lead to BLH uncertainties, as the cumulus cloud top heights are
26 often higher than the BLH. Those issues could result in statistical biases in marine BLH
27 distributions differences in reported values and spatial distributions of the BLH over ocean
28 among early studies.

29 After considering the MBL decoupling structure, a new CALIOP based approach was
30 developed to reliably determine BLH and MLH in order to investigate the clear-sky MBL
31 decouple structure (Luo, et al., 2014a). This study uses this new method to investigate the
32 MBL decouple structure over the eastern Pacific Ocean region using CALIOP observations,

1 and combining CloudSat observations with reliable cloud type identification to provide BLH
2 information under stratiform-cloud-topped conditions. The authors also present an
3 examination of the dependence of the MBL decoupled structure on environmental parameters
4 over global oceans. Section 2 describes the data used in this study. Section 3 introduces and
5 evaluates the lidar MBL structure identification methodology with the ship-base observations.
6 Section 4 presents the results and discussions, and brief conclusions are in section 5.

7 **2 Data**

8 **2.1 Satellite Observations and Data Collocation**

9 This study uses multiple remotely sensed and operational meteorological datasets over global
10 oceans during the period from June 2006 to December 2010.

11 Clear-sky MBL structure was determined from the cloud-free CALIOP measured aerosol
12 backscattering with the cloud-free condition defined as no cloud below 8km, although cases
13 with optically thin high clouds above 8km are included. CALIOP is a dual-wavelength (532
14 and 1064 nm) backscatter lidar, which is carried on the Cloud-Aerosol Lidar and Infrared
15 Pathfinder Satellite Observations (CALIPSO) (Winker et al., 2007; Winker et al., 2009). At
16 532 nm, the CALIOP provides both the parallel and perpendicular polarization components of
17 attenuated backscatter. The along-track footprint of CALIOP is 333m with the vertical
18 resolution of 30m below 8.2 km. CALIOP level 1B data provide three calibrated and geo-
19 located lidar profiles of 532nm and 1064nm total attenuated backscatter (TAB) and 532nm
20 perpendicular polarization component. The molecular backscattering was estimated using the
21 temperature and pressure profiles from the ECMWF-AUX (European Center for Medium
22 range Weather Forecasting AUX-algorithm, Partain, 2004).

23 CloudSat carries a 94 GHZ cloud profiling radar (CPR) (Stephens et al., 2002). The CloudSat
24 antenna pattern provides an instantaneous footprint at mean sea level of approximately 1.3
25 km, while vertically it has 125 bins with a bin size of about 240m. Cloud top height (CTH)
26 and cloud type were obtained from the 2B-CLDCLASS-LIDAR product (Wang et al., 2012;
27 Sassen and Wang 2012) with combining CloudSat and CALIOP observations, allowing better
28 identify the cloud boundaries. In order to produce clear-sky aerosol information, cloudy
29 CALIOP profiles were removed from further averaging. And the cloudy BLH was estimated
30 from the CTH of marine stratiform clouds, which was a good proxy for estimating the marine
31 BLH under cloudy conditions and has been widely used in the previous studies (Minnis et al.

1 1992; Wood and Bretherton 2004; Ahlgrimm and Randall 2006; Zuidema et al. 2009;
2 Karlsson et al., 2010). Classification of drizzle within the Cloudy MBL was performed by
3 applying a threshold of -20 dB (Leon et al., 2008) to the CloudSat CPR measured reflectivity
4 factor in CloudSat 1B-CPR product (Tanelli et al., 2008).

5 The atmospheric large-scale stability parameters used in this study include lower tropospheric
6 stability (LTS) (Klein and Hartmann 1993), and estimated inversion strength (EIS) (Wood
7 and Bretherton 2006). LTS is calculated using the difference in potential temperature between
8 700 hPa and the surface ($\theta_{700} - \theta_{\text{surface}}$), whereas EIS is the difference between LTS and $\Gamma_{850} *$
9 ($Z_{700} - \text{LCL}$), where, Γ_{850} is the moist adiabatic lapse rate at 850hPa, LCL is lifting
10 condensation level, and Z_{700} is the height at 700hPa. EIS is considered a more precise
11 measure of the strength of a possible inversion than the LTS. EIS and LTS were estimated
12 from AIRS (the Atmospheric Infrared Sounder) level 2 version 5 products (Jason, 2008).
13 AIRS is a grating spectrometer carried on Aqua. It has a spectral resolution of $\nu/\Delta\nu \approx 1200$, a
14 total of 2378 channels in the range of 3.7–15.4 μm with a few spectral gaps, and provides
15 well-calibrated level 1B radiances (Overoye, 1999). AIRS is co-registered with AMSU
16 (Pagano et al., 2003; Lambrightsen and Lee, 2003), and the combined measurements are used
17 to retrieve temperature, humidity and numerous other surface and atmospheric parameters.
18 Geophysical retrievals are obtained in clear sky and broken cloud cover through the use of a
19 cloud-clearing methodology (Susskind et al., 2003). Though there is no retrieval under
20 overcast conditions, AIRS can provide a reasonable measure of the seasonal mean EIS as
21 compared to model simulations (Yue et al., 2001). Additionally, the AIRS-derived EIS has
22 strong connection with low cloud (Yue et al., 2001), making the, seasonal-mean EIS
23 appropriate for the analysis of the MBL cloud behaviors in this paper.

24 The sea surface temperature (SST) and surface wind speed at 10m (U_{10m}) were obtained from
25 AMSR-E Level 3 daily Ocean Products version-7 (Wentz et al., 2014). The Advanced
26 Microwave Scanning Radiometer - Earth Observing System (AMSR-E) is a twelve-channel,
27 six-frequency, passive-microwave radiometer system (Kawanishi et al, 2003). It measures
28 horizontally and vertically polarized brightness temperatures at 6.9, 10.7, 18.7, 23.8, 36.5, and
29 89.0 GHz. Spatial resolution of the individual measurements varies from 5.4 km at 89 GHz to
30 56 km at 6.9 GHz. AMSR-E is co-located with AIRS and AMSU onboard Aqua and in the A-
31 train with CALIPSO; thus, the instruments are sampling similar conditions and the same time
32 of day. The daily AMSR-E Ocean Products are produced by Remote Sensing Systems (RSS,

1 http://www.remss.com/). The orbital data is mapped to 0.25° grid box and is divided into 2
2 maps based on ascending and descending passes for daytime and nighttime orbits. Error in the
3 data was estimated using the root mean square (RMS) difference between AMSR-E U_{10m} and
4 U_{10m} coming from four other satellite microwave radiometers (three SSM/Is and TRMM
5 TMI) and with U_{10m} from the satellite microwave scatterometer QuikScat (0.92 m/s with a
6 bias of 0.57 m/s) (Wentz et al., 2003). This calculation gave an RMS difference between
7 AMSR-E SST retrievals and the Reynolds SST as 0.76 K (Wentz et al., 2003). Validation
8 using data from a buoy (National Data Buoy Center, NDBC) U_{10m} (mean value of 6.61 m/s)
9 gave an RMS difference with AMSR-E U_{10m} (mean value of 6.46 m/s) is 1.63 m/s with a bias
10 of -0.15 m/s (Luo et al., 2015). Validation with NDBC buoy SST (mean value of 299.49 K)
11 in this study showed that the RMS difference in AMSR-E SST (mean value of 299.26 K) is
12 0.99 K with a bias of -0.23 K .

13 All the related datasets were collocated into AMSR-E 0.25° grid-box and cloud-free CALIOP
14 backscattering profiles are then averaged. CALIOP backscattering profiles with no cloud
15 below 8 km (including cases with clouds above 8 km) were averaged. Thus, within each 0.25°
16 grid-box, there are three general conditions of the MBL: 100% cloud cover, partial cloud
17 cover, and cloud-free. For the 100% cloud cover the BLH is determined from stratiform CTH.
18 For the partial cloud cover, and cloud-free conditions the daily day- or night- averaged cloud-
19 free CALIOP measurements are used to determine BLH and MLH. The following analyses
20 only present data taken over the oceans (within 50°N and 50°S , and at least 200 km away from
21 continental boundaries), but include both daytime and nighttime observations. The MBL
22 aerosol identifications are the same as in Luo et al. (2014a).

23 **2.2 MAGIC and Collocated Satellite Observations**

24 The Marine ARM GPCI (GCSS Pacific Cross-section Intercomparison, a working group of
25 GCSS; GCSS is GEWEX Cloud Systems Study) Investigation of Clouds (MAGIC) field
26 campaign (<http://www.arm.gov/sites/amf/mag/>) deployed the U.S. Department of Energy
27 (DOE) Atmospheric Radiation Measurement Program Mobile Facility 2 (AMF2) on the
28 commercial cargo container ship Horizon Spirit from October 2012 through September 2013
29 with 20 round trips (Lewis et al., 2012; Zhou et al., 2015). The MAGIC transect is the line
30 from the coast of California to Hawaii (35.8°N , 125.8°W to 18°S , 173.8°W) and was
31 undertaken to provide unprecedented, intra-seasonal, high-resolution ship-based observations
32 in order to improve the understanding of the Sc-to-Cu (Stratocumulus-to-Cumulus) transition

1 along this transect. The AMF2 contained a state-of-the-art instrumentation suite and was
2 designed to operate in a wide range of climate conditions and locations, including shipboard
3 deployments.

4 This study used atmospheric soundings and MARMETX (marine meteorological
5 measurements) datasets to characterize MBL structure. Standard radiosondes (Vaisala model
6 MW-31, SNE50401) were launched every 6-hour to measure vertical profiles of the
7 thermodynamic state of the atmosphere (temperature, pressure, relative humidity, and wind
8 speed and direction). The MARMETX dataset
9 (<http://www.arm.gov/campaigns/amf2012magic/>) contains standard surface meteorological
10 parameters measured by the MARMET: temperature (T), pressure (P), relative humidity
11 (RH), and apparent and true wind speed and direction; and the sea surface skin temperature
12 measured by the Infrared Sea surface Temperature Autonomous Radiometer (ISAR) with an
13 accuracy of better than 0.18°C.

14 The high spectral resolution lidar (HRSL, Shipley et al., 1983; Piironen and Eloranta, 1994)
15 measuring total attenuated backscattering was also used to document the aerosol and cloud
16 distributions. Because of the high occurrence of the cloud along the MAGIC transect, the
17 lidar-based MBL structure identification method was not applied to the HRSL observations.

18 To evaluate the satellite-retrieved MBL structure with results from MAGIC soundings, the
19 cloud-free CALIOP observations within a 2.5° grid-box and within 1 day of MAGIC
20 soundings during October 2012 through September 2013 were collocated. The loose
21 restriction was applied in the collocation, because limited MAGIC soundings, poor spatial
22 coverage of CALIOP measurements, and high occurrence of clouds in the region. The cloud-
23 free CALIOP profiles were firstly averaged into 0.25° grid-box to improve the signal-to-noise
24 ratio. Then the MBL structure were identified and averaged into the 2.5° grid-box.

25

26 **3 MBL Structure Identification Methodology**

27 **3.1 MBL structure identification methodology for radiosonde**

28 For radiosonde, the BLH was determined by the Richardson number (RI) method (with the
29 Eq. (2) in Vogelegang and Holtslag, 1996). This method determines the BLH as the height at
30 where RI is larger than the critical value (= 0.25). The RI method is suitable for both stable

1 and convective boundary layers. This method gives the BLH more physical meaning as it
2 relates the derived BLH to boundary layer processes - surface heating, wind shear and
3 capping inversion. Also, RI method does not produce a negative BLH, as it does not depend
4 strongly on the sounding vertical resolution of the sounding. Therefore, the RI method is
5 often considered as the best estimation against which to evaluate lidar based BLH estimations
6 (Hennemuth and Lammert, 2006; Seidel et al, 2010).

7 Figure 1 presents one transect HSRL and potential temperature from MAGIC measurements.
8 It is clear that the BLHs from the RI method correspond well with the aerosol layer tops, or
9 stratiform clouds tops over the stratiform cloud region (eastern than longitude of $\sim 137^\circ$).
10 There is also some correspondence of BLHs with the highest cumulus clouds tops over the
11 cumulus cloud region (western than longitude of $\sim 137^\circ$). Over the cumulus cloud region the
12 MBL becomes obviously decoupled, and there is usually one or more weak inversion layers
13 below the RI determined BLH. The lowest inversion layer usually limits the upward
14 transportation of the aerosols to form a layer, forming a layer with more concentrated aerosols
15 than that above (this can also be seen in Figure 4 in Luo et al. (2014a)). This inversion can also
16 limit the vertical developments of the small cumulus clouds that may form in the mixing
17 layer. This characteristic allows the identification of MLH height as the base of the lowest
18 inversion layer with inversion strength larger than $0.05\text{K}/100\text{m}$ in radiosonde potential
19 temperature profiles. This threshold was chosen based on visual check of all MAGIC
20 transects.

21 **3.2 MBL structure identification methodology for CALIOP**

22 As detailed in Luo et al. (2014b), the BLH can be determined with an improved threshold
23 method using a threshold $\beta'_{thr} = \beta'_m + 2 * MBV$ applied to the marine aerosol backscattering
24 coefficient profile retrieved from collocated CALIOP level 1B data. In this equation, β'_m is
25 the molecular backscattering coefficient, estimated by temperature and pressure profiles from
26 ECMWF-AUX products; MBV is the measured backscatter variation, estimated as the
27 standard deviation of measured attenuated backscatter coefficients from 30 to 40 km.

28 The MLH was identified by the gradient method (Luo et al., 2014a). The gradient of aerosol
29 backscattering coefficient is calculated after three points moving average smoothing. After
30 smoothing, the MLH is determined to be the lowest point with an aerosol backscattering
31 coefficient gradient larger than 2 times of the molecular backscattering gradient.

1 The evaluation of lidar methodology with radiosonde soundings were performed with 2-year
2 (2007-2008) clear-sky Atmospheric Radiation Measurement Program (ARM) Climate
3 Research Facility (ACRF) radiosonde and micro pulse lidar (MPL) observations (Xie et al.,
4 2010, Mather and Voyles, 2013) collected from Nauru (marine site). Detailed data process
5 can be found in Luo et al. (2014a). When compared to radiosonde-derived BLH, the bias and
6 root mean square error (RMSE) of MPL derived BLH is -0.12 ± 0.24 km with a correlation
7 coefficient of 0.75. When compared to radiosonde-derived MLH, the bias and RMSE of MPL
8 derived MLH is -0.06 ± 0.16 km with a correlation coefficient of 0.66. An overall
9 comparison of radiosonde-derived to MPL derived MLH/BLH produces a bias and RMSE of
10 -0.02 ± 0.1 and a correlation coefficient between of 0.61. All the correlation coefficients are
11 reported at confidence level of 0.01. These small values of mean bias indicate that our
12 CALIOP based BLH and MLH determinations for clear-sky MBL can be considered accurate.
13 Further evaluations were performed with loosely collocated CALIOP and MAGIC
14 observations. While only cloud-free CALIOP profiles can be used to derive the MBL
15 structure, the soundings were measured in all-sky conditions (mostly cloudy conditions) (Fig.
16 1). Figure 2 shows the comparisons of MBL structure between radiosonde and CALIOP
17 measurements. The mean MBL structure by CALIOP and radiosonde along the MAGIC
18 transect is shown in Fig. 2 (a). Both results show a similar trend in the MBL structure, being
19 less decoupled near the coast and more decoupled over the far ocean. The heights of the
20 CALIOP-derived BLH and MLH are lower than those derived from the radiosonde. Over the
21 stratiform cloud regions, the CALIOP-derived MBL structure appears more decoupled than in
22 the radiosonde results. However, the CALIOP-derived BLH shows good agreement with
23 those from radiosonde as shown in Fig. 2 (b). The bias and RMSE in CALIOP-derived BLH
24 were calculated to be -0.14 ± 0.37 km, with a correlation coefficient of 0.56 at the confidence
25 level of 0.01. For CALIOP-derived MLH, the bias and RMSE is -0.1 ± 0.45 km with a
26 correlation coefficient of 0.34 at the confidence level of 0.01. Although the biases are small,
27 the RMSE differences are large, mainly as a result of limited sampling and large spatial
28 mismatch, and different cloud conditions. This is especially true over the stratiform cloud
29 region where the cloud fraction in the MBL is very high (Fig. 1). In this area the collocated
30 cloud-free CALIOP profiles are often too far from the sounding observations to produce a
31 strong correlation. However, Fig. 2 clearly shows that the CALIOP-observed clear-sky MBL
32 structure captures a similar spatial trend as those from the nearby cloudy-sky MBL.

1 Additionally, the radiosonde-derived MLH agrees well with the LCL (Fig. 2(b)), with the bias
2 and RMSE of -0.13 ± 0.21 km, and with a correlation coefficient of 0.73 at the confidence
3 level of 0.01. Figure 2(d) shows that the CALIOP-derived BLH and stratiform CTHs (CTH_{sc})
4 within the same AMSR-E grid box over the eastern Pacific Ocean region show good
5 agreements, with the bias and RMSE of -0.06 ± 0.52 km, and with a correlation coefficient of
6 0.66 at the confidence level of 0.01. Good agreement between the CALIOP-derived BLH and
7 CTH_{sc} can also be found over the global oceans (Luo et al., 2014a).

8 **4 Results and Discussions**

9 **4.1 MBL Structure over the Eastern Pacific Ocean**

10 This section uses the 4-year new MBL and marine boundary layer cloud (MBLC) dataset
11 described in the previous to investigate the MBL structure over the eastern Pacific. The
12 MBLC dataset includes cloud type and stratiform-cloud (Sc) top and drizzle information
13 based on the CloudSat products. Figure 3 shows the 4-year mean MBL structure (BLH, MLH
14 and MLH/BLH), CTH_{sc} (with or without drizzle), EIS and U_{10m} over the eastern Pacific
15 Ocean. Hereafter, the MBL structure (BLH, MLH and MLH/BLH) is referred to the clear-sky
16 condition with aerosols as a proxy, while the CTH_{sc} is used as the proxy of BLH under
17 cloudy conditions.

18 The 4-year mean BLH over the eastern Pacific Ocean is shown in Fig. 3 (a). Fig. 3 (a) shows
19 that the marine BLH is lower than ~ 1 km near the coast region at latitude of $\sim \pm 30^\circ$. This is
20 assumed to due to the strong subsidence and low SST. When moving away from the strong
21 subsidence region, the BLH increases. The BLH is highest over the Intertropical Convergence
22 Zone (ITCZ) attributed to large-scale convergence and the high SST causing strong
23 buoyancy-driven vertical turbulence mixing. This is especially prevalent over the eastern
24 Pacific near the Central America. However, the BLH is low along the equator with a tendency
25 to rise heading westward. The 4-year mean MLH (Fig. 3(b)) shows a similar spatial pattern as
26 the BLH, with a correlation coefficient of 0.6 at confidence level of 0.01. The rising trend of
27 BLH when away from the coast was also illustrated in former satellite-based studies (Ratnam
28 and Basha, 2010; Guo et al, 2011; Ao et al, 2012Randall et al., 1998; Palm et al., 2005;
29 Jordan et al., 2010; McGrath-Spangler and Denning, 2012, 2013). However, due to different
30 methodologies associated with different definition of BLH and the filtering of cloud
31 conditions, this study shows a significant magnitude of differences in BLH form former

1 studies. As an example, the BLH reported in McGrath-Spangler and Denning (2013) is much
2 lower than the BLH seen in our results, but there is similarity in pattern and value of our
3 MLH and the McGrath-Spangler and Denning BLH over the eastern Pacific Ocean.

4 The 4-year mean MBL coupling status in terms of averaged ratio of MLH/BLH is shown in
5 Fig. 3 (c). The better mixed the MBL, the larger the ratio of MLH/BLH. This is shown in the
6 stratiform cloud dominated region (where Sc Fraction $> \sim 0.4$ with stronger EIS and lower
7 BLH) where there is higher MLH/BLH than in the cumulus cloud dominated region (where
8 Sc Fraction $< \sim 0.4$ with weaker EIS and higher BLH). The MBL is obviously decoupled over
9 the ITCZ. The MBL shows better mixing from 100°W to 80°W of the equator, but weak
10 mixing from 160°W to 100°W of the equator. And the decoupling trend of the MBL is present
11 westward along the equator.

12 Sc occurs more frequently (Sc fraction $> \sim 0.6$) when EIS $> \sim 1K$, with a decreasing fraction
13 towards the far ocean, as shown in Fig. 3 (d). Sc occurrence depends on the EIS (Fig. 3 (g)),
14 with a correlation coefficient of 0.78 at confidence level of 0.01 in their spatial patterns.
15 Figures 3 (e) and (f) show Sc tops with and without drizzle. The Sc case is defined as the case
16 where there are only Sc (and clear-sky if it has) profiles in the collocated 0.25° grid-box (the
17 Sc fraction > 0). These cases are then broken into the Sc case with and without drizzle. The Sc
18 case with drizzle is the Sc case where at least one Sc profile in the collocated 0.25° grid-box
19 has drizzle, while the remaining Sc cases are non-drizzled Sc case. The drizzled Sc tops are
20 lower than ~ 1.5 km when near the coast where the stratus cloud is dominant, and the drizzled
21 Sc tops rise up to ~ 2.5 km as distance away from the coast increases. The non-drizzled Sc
22 tops show a similar pattern to the drizzled Sc top (with a correlation coefficient of 0.53 at
23 confidence level of 0.01 in their spatial pattern), except that the non-drizzled Sc top are lower
24 when approaching the tropical Pacific near longitude of $\sim 180^{\circ}$ W. Generally, the drizzled Sc
25 top is ~ 0.2 to 1 km higher than the non-drizzle Sc top, which suggests the important role of
26 the mesoscale circulations in MBL. Precipitation more commonly occurs in updraft regions
27 and the breakup of Sc usually happens in downdrafts areas, which was also observed in the
28 rift area of Sc (Sharon et al., 2006) and in MAGIC (Zhou et al., 2015). Furthermore, the
29 occurrence of drizzled Sc case is $\sim 6.2\%$ (the number of Sc profiles with drizzle / the number
30 of Sc profiles) among MBL cases where a 0.25° grid-box contains both Sc and clear-sky,
31 comparing to $\sim 32\%$ of all MBL cases being stratiform cloud with drizzle cases. The Sc case
32 containing clear-sky profiles are where broken Sc clouds or a cloud edge enter a 0.25° grid-

1 box. This relationship indicates that heterogeneous cloudy conditions within a grid-box (i.e.,
2 broken Sc clouds or near the cloud edge) are less likely to produce precipitation than where
3 the conditions are more homogeneously cloudy.

4 The detailed assessments of the seasonal MBL and MBLC structures in the two selected
5 transects over the northeastern and southeastern Pacific Ocean (NPO and SPO) are presented
6 in Figs. 4 and 5. Figs. 4 and 5 (a1-a4) show the seasonal mean MBL structure in terms of
7 MBL aerosol loading, overlain with seasonal mean BLH and MLH. The mean BLH, MLH
8 and their standard deviations, show that the MBL tends to be more frequently well mixed near
9 the coast region and be more frequently decoupled over the far ocean. This corresponds to a
10 stronger EIS near the coast and weaker EIS over the far ocean (the black diamond-solid lines
11 in Figs. 4 and 5 (b1-b4)). The EIS over the NPO shows negative correlation with the U_{10m} ,
12 with a correlation coefficient of -0.64 at confidence level of 0.01, but there is a positive
13 correlation with the U_{10m} when EIS < 3 K over the SPO, with the correlation coefficient of 0.6
14 at confidence level of 0.01. The seasonal variations in the MBL structure are small over both
15 the NPO and SPO regions, except that the MBL tends to be lower and better mixed near the
16 coast region during March, April and May (MAM) and June, July and August (JJA) over the
17 NPO, and in JJA and September, October and November (SON) over the SPO. This is likely
18 associated with the stronger EIS (> 5 K) in these seasons than EIS (< 5 K) in the other
19 seasons.

20 Surface wind speed is the main factor controlling the loading of sea salt aerosols near the
21 surface, while its vertical distribution is closely related to the boundary layer processes (Luo
22 et al., 2014b). When distant away from the coast, the aerosol loading (Figs. 4 and 5 (a1-a4)) in
23 the well-mixed layer shows strong positive correlation with the U_{10m} in NPO with a
24 correlation coefficient of 0.64 at the confidence level of 0.01. However, there is almost no
25 correlation between them in the SPO (correlation coefficient of -0.08 at the confidence level
26 of 0.39). In the SPO, when further east than longitude of $\sim 100^\circ$, the aerosol loading in the
27 lower well-mixed layer increases with decreasing of the U_{10m} . This is attributed to lowering
28 MLH limiting the vertical transportation. When near the coast region, the aerosol loading in
29 the well-mixed layer has weak correlation with the U_{10m} over both regions, possibly due to the
30 aerosol transported from the continent.

31 Figures 4 and 5 (c1-c4) show the mean Sc occurrences over the two regions. Over the NPO
32 region (Fig. 4 (c1-c4)), the Sc occurrence is small near the coast and increases to a maximum

1 of ~ 0.6 near the longitude of $\sim 130^\circ$ to -135° . It then decreases when west southward towards
2 the tropic. Over the NPO, the Sc occurrence increases with decreasing of EIS when distant
3 from the coast to the maximum occurrence point (at longitude of $\sim 135^\circ$), with the correlation
4 coefficient of -0.51 at the confidence level of 0.01 . And there shows a positive correlation
5 with EIS from the maximum occurrence point down to the equator, with the correlation
6 coefficient of 0.92 at the confidence level of 0.01 . Over the SPO region (Fig. 5 (c1-c4)), the
7 maximum Sc occurrence point is close to the coast. Therefore, the Sc occurrence and the EIS
8 both decrease when far away from the coast and correlate well with each other when further
9 west than longitude of $\sim 80^\circ$, with the correlation coefficient of 0.91 at the confidence level of
10 0.01 . In the near-coast region, other processes such as sea-land breeze and cold current
11 producing cold SST could affect the relationship between EIS and Sc occurrence. The drizzle
12 occurrence showed a weak correlation with EIS in both regions (not shown here).

13 Figures 4 and 5 (d1-d4) show the seasonal mean $CTH_{drizzle}$ (blue diamond line) and $CTH_{no drizzle}$
14 (green diamond line) along with the seasonal mean BLH and MLH over the NPO and
15 SPO. The $CTH_{no drizzle}$ is lower than the $CTH_{drizzle}$, but is close to the BLH. Over the NPO
16 region, the $CTH_{drizzle}$ shows strong negative correlation with the EIS, with the correlation
17 coefficients of < -0.82 at the confidence level of 0.01 . Over the NPO region, in MAM, JJA
18 and SON, the $CTH_{drizzle}$ shows strong negative correlation with the EIS, with the correlation
19 coefficients of < -0.77 at the confidence level of 0.01 , while very weak correlation in
20 December, January and February (DJF), with the correlation coefficients < -0.33 at the
21 confidence level of 0.08 . The $CTH_{no drizzle}$ generally shows a weak correlation with the EIS,
22 although there is a positive correlation with the EIS for sub-regions, such as over the SPO
23 when west of longitude of $\sim -90^\circ$ in DJF and MAM and when west of longitude of $\sim -100^\circ$ in
24 JJA and SON, with the correlation coefficients of > 0.64 at the confidence level of 0.01 . The
25 difference between $CTH_{drizzle}$ and $CTH_{no drizzle}$ shows strong dependence on the EIS, i.e., there
26 is a smaller difference associated with stronger EIS and larger difference associated with
27 weaker EIS. This is attributed to a stronger EIS indicating a more stable MABL, which allows
28 for small depth variations associated with several possible vertical displacement forces in
29 MBL. Thus, a small difference between $CTH_{drizzle}$ and $CTH_{no drizzle}$ is expected under stronger
30 EIS.

31 The MBL activities are strongly connected with the large-scale stabilities. Figure 6 shows the
32 relationships between EIS and MBL coupling structure. In Fig. 6 (a), MAGIC observations

1 and CALIOP observations over the extended MAGIC region were sorted and averaged into
2 different bins of EIS. Both observations from MAGIC radiosonde and CALIOP show that the
3 MBL tends to be better mixed as EIS increases. One of the main parameters controlling the
4 entrainment process is the inversion strength near the mixing layer top (Venzenten et al.,
5 1999). According to the definition of EIS, it implies that a stronger EIS leads to a stronger the
6 inversion near the mixing layer top, and a weaker the entrainment of the dry warm air above
7 the inversion. Therefore, the relationship between EIS and MBL structure indicates that the
8 entrainment of the dry warm air above the inversion would be the main factor controlling the
9 MBL decoupling. It could also be expected that the SST, wind shear and surface heat flux
10 may also affect MBL decoupling as these parameters or processes can also affect the
11 entrainment process (Venzenten et al., 1999). However, analyses of U_{10m} and SST show only
12 very weak correlations with MBL coupling structure. This is possibly due to the uncertainties
13 in satellite retrievals of these parameters or that the role of other factors was partially included
14 in the EIS.

15 After further investigation, we concluded that the MBL coupling structure is controlled by
16 both LTS and EIS when $EIS < \sim 3$ K, i.e., there is greater mixing in the MBL with increasing
17 EIS and decreasing of LTS. Fig. 6(b) shows the mean CALIOP-derived MBL coupling
18 structure over global oceans under binned EIS and LTS values. As shown in Fig. 6(b), the
19 mean MBL coupling structure in terms of MLH/BLH shows good correlation with EIS under
20 different bins of LTS when LTS is between 2.5K and 17.5K (correlation coefficient of > 0.88
21 at confidence level of 0.01). And the MBL coupling structure in term of MLH/BLH shows a
22 very strong negative correlation with LTS when binned $EIS < 2$ K (correlation coefficient < -0.95
23 at confidence level of 0.01).

24 The differences between drizzling and non-drizzling Sc tops are also controlled by the EIS.
25 Figure 6(c) shows the seasonal mean relationship over the global oceans between EIS and
26 $CTH_{no\ drizzle}/CTH_{drizzle}$ binned by SST. The SST, EIS and $CTH_{no\ drizzle}/CTH_{drizzle}$ was averaged
27 across a $2.5^{\circ} \times 2.5^{\circ}$ grid box and different seasons. After this, the seasonal-mean $CTH_{no\ drizzle}/CTH_{drizzle}$
28 was sorted and averaged into different bins of EIS and SST. This binning
29 showed that wth cold SST ($SST < = 20^{\circ}C$) in the middle to high latitude regions, mean $CTH_{no\ drizzle}/CTH_{drizzle}$
30 does not vary with EIS, whereas in the Sc-to-Cu transition regions where there
31 is warm SST ($SST > 20^{\circ}C$), the mean $CTH_{no\ drizzle}/CTH_{drizzle}$ shows good dependence on EIS (a
32 correlation coefficient > 0.89 at confidence level of 0.01). The relative difference between

1 CTH_{drizzle} and CTH_{no drizzle} becomes larger with decreasing EIS and increasing SST, indicating
2 more vigorous the subsidence and uplifting in the MBL under weak EIS conditions and
3 warmer SST. This result suggests that the subsidence and uplifting may relate to meso-scale
4 processes, such as gravity waves, which can be generated from the geostrophic adjustment, jet
5 break or other sources, affecting the morphology of clouds (Jiang and Wang, 2012; Allen et
6 al., 2013) over the Sc-to-Cu transition regions. The different roles of SST and EIS in
7 controlling Sc top and precipitation generation in different regions will be further investigated
8 of in future studies.

9 **4.2 Discussion**

10 The MBL decoupling was suggested to play an important role in Sc-to-Cu transition
11 (Bretherton and Wyant, 1997; Wood and Bretherton, 2004). The MBL structure is shown in
12 Fig. 7 as the mean of aerosol backscattering from the cases with both clear-sky and
13 stratiform/Cu cloud in the same 0.25° grid box over the eastern Pacific Ocean where the Sc-
14 to-Cu transition frequently happens. The clear condition is defined as totally cloud-free in the
15 25 km AMSR-E footprint (named as clear MBL). This condition is expected to be less
16 affected by the local circulation associated with the cloud development. Aerosols under the
17 stratiform cloud condition are derived from cases with partially stratiform cloud and partially
18 clear sky in a 0.25° AMSR-E footprint (named as stratiform MBL). Aerosols under the Cu
19 cloud condition are derived from cases with partially Cu cloud and partially clear sky in a
20 0.25° AMSR-E footprint (named as Cu MBL). According to the comparison of CALIOP-
21 derived clear-sky MBL structure with near-by cloudy-sky MBL structure from MAGIC
22 radiosonde and with the nearby stratiform cloud top from 2B-CLDCLASS-LIDAR in section
23 3.2, it is reasonable to assume that the cloud-topped MBL can have the similar structure to the
24 nearby clear-sky MBL within a 0.25° footprint for the Sc and Cu MBL cases. Figure 7 shows
25 that the clear MBL and Cu MBL become more decoupled with increasing BLH and
26 decreasing EIS as indicated by large vertical gradients between mixing layer aerosols and near
27 MBL top aerosols. The Stratiform MBL shares similar characteristics to the Cu MBL, but are
28 better mixed than clear MBL and Cu MBL when EIS > 0. According to Fig. 3, the region with
29 EIS < 0 K is the Cu cloud dominated region (where the fraction of Sc cloud is smaller than
30 0.2), and the Sc MBL cases here are more likely to associated with the clear-sky MBL
31 adjacent to the small Sc. The region of 0 K < EIS < 2.5 K is considered a transition region
32 where the Sc clouds are broken down and transit to Cu clouds. The Stratiform MBL cases

1 with $0 \text{ K} < \text{EIS} < 2.5 \text{ K}$ are more likely associated to the clear-sky MBL adjacent to broken Sc.
2 The stratiform MBL cases with $\text{EIS} > 2.5 \text{ K}$ are more likely associated with the clear-sky
3 MBL near the edge of overcast Sc in the region where Sc fraction $>\sim 0.6$. When $\text{EIS} < 0\text{K}$, the
4 stratiform MBL showed no major difference between clear MBL and Cu MBL. With
5 increasing EIS, corresponding to increasing amount of stratiform clouds, the presence of
6 large-scale subsidence prompts a well-mixed MBL, or more occasionally a decoupled MBL
7 with two well-mixed sub-layers (Fig. 7(c2)).

8 **5 Conclusions**

9 This paper used 4-year satellite observations to investigate the MBL decoupled structure and
10 its spatial distribution over the eastern Pacific region and its dependence on environmental
11 parameters over global oceans (within latitude of $\pm 50^\circ$). The aerosol information in CALIOP-
12 measured backscattering data is considered to be a good proxy for the MBL decoupled
13 structure. The aerosol layer top is a good indicator for BLH and was able be identified by the
14 threshold method, whereas the MLH could be identified by the gradient methods. The lidar
15 determined BLH showed good agreements with BLH determined by the RI method using
16 radiosonde measurements and with the stratiform cloud top from CloudSat product. The lidar
17 determined MLH showed good agreement with the base of lowest inversion layer in
18 radiosonde temperature profiles.

19 The lidar methodology was then applied to the 4-year satellite observations over the eastern
20 Pacific Ocean. Clear-sky MBL structure characteristics were analyzed together with the
21 cloudy MBL top (inferred from the stratiform cloud top). For the first time, the climatology
22 and seasonal variations of the MBL structure in the eastern Pacific Ocean region were
23 presented and analyzed. This analysis showed that MBL is generally decoupled, with
24 MLH/BLH ratio ranging from ~ 0.5 to ~ 0.8 . The MBL decoupling magnitude is mainly
25 controlled by EIS that affects the cloud top entrainment process, with correlation coefficient
26 of > 0.88 at confidence level of 0.01 between the mean MBL coupling structure in terms of
27 MLH/BLH and EIS when binned LTS is between 2.5K and 17.5K. The systematic differences
28 between drizzling and non-drizzling Sc tops over the Sc-to-Cu transition region also show
29 dependence on EIS and may relate to the meso-scale circulations driven by gravity wave in
30 MBL. Further analysis showed that the MBL shows similar decoupled structure under clear
31 sky and cumulus cloud-topped conditions, but is better mixed under Sc breakup and overcast
32 conditions.

1 This study demonstrated that satellite lidar measurements offer a unique opportunity to
2 characterize MBL over global oceans, something no possible using other techniques. Multi-
3 satellite measurements also offer a chance to further study related MBL processes. Using
4 observational results presented here, it will be possible to evaluate and improve model MBL
5 simulations under different dynamical and thermodynamical conditions.

6 **Acknowledgements**

7 This research was partially funded by the DOE Grant DE-SC0006974 as part of the ASR
8 program and by the NASA Grant NNX13AQ41G. We would also like to thank anonymous
9 reviewers for their positive and constructive comments. The authors would like to thank
10 CloudSat team for providing data from the CloudSat Data Processing Center
11 (<http://www.cloudsat.cira.colostate.edu>). The authors would like to thank the CALIOP team
12 for providing data obtained from the NASA Langley Research Center Atmospheric Science
13 Data Center. AMSR data are produced by Remote Sensing Systems and were sponsored by
14 the NASA AMSR-E Science Team and the NASA Earth Science MEaSUREs Program and
15 are available at www.remss.com. AIRS data were obtained through the Goddard Earth
16 Sciences Data and Information Services Center (<http://daac.gsfc.nasa.gov>). The buoy data was
17 obtained from National Data Buoy Center (<http://www.ndbc.noaa.gov/>). ARM data is made
18 available through the U.S. Department of Energy as part of the Atmospheric Radiation
19 Measurement (ARM) Program. ARM Climate Research Facility TWP-C2 site data and
20 MAGIC campaign data were used.

21

1 **References**

2 Ahlgrimm, M. and Randall, D. A.: Diagnosing monthly mean boundary layer properties from
3 reanalysis data using a bulk boundary layer model, *J. Atmos. Sci.*, 63, 998-1012, 2006.

4 Ao, C. O., Waliser D. E., Chan, S. K., Li, J.-L., Tian, B., Xie, F., and Mannucci, A. J.:
5 Planetary boundary layer heights from GPS radio occultation refractivity and humidity
6 profiles, *J. Geophys. Res.*, 117, D16117, 2012.

7 Albrecht, B. A., Jensen, M. P., and Syrett, W. J.: Marine boundary layer structure and
8 fractional cloudiness, *J. Geophys. Res.*, 100(D7), 14209-14222, 1995.

9 Allen, G., Vaughan, G., Toniazzo, T., Coe, H., Connolly, P., Yuter, S. E., Burleyson, C. D.,
10 Minnis, P., and Ayers, J. K.: Gravity-wave-induced perturbations in marine stratocumulus,
11 *Quarterly Journal of the Royal Meteorological Society*, 139 (670), 32-45, 2013.

12 Bony, S. and Dufresne, J.-L.: Marine boundary layer clouds at the heart of tropical cloud
13 feedback uncertainties in climate models, *Geophys. Res. Lett.*, 32, L20806, 2005.

14 Boers, R., Eloranta, E. W., and Coulter, R. L.: Lidar observations of mixed layer dynamics:
15 tests of parameterized entrainment models of mixed layer growth rate, *J. Clim. Appl.*
16 *Meteorol.*, 23, 247-266, 1984.

17 Boers, R. and Eloranta, E. W.: Lidar measurements of the atmospheric entrainment zone and
18 potential temperature jump across the top of the mixed layer, *Bound.-Lay. Meteorol.*, 34, 357-
19 375, 1986.

20 Bretherton, C. S. and Wyant, M. C.: Moisture transport, lower-tropospheric stability, and
21 decoupling of cloud-topped boundary layers, *J. Atmos. Sci.*, 54, 148-167, 1997.

22 Emeis, S., Schafer, K., and Munkel, C.: Surface-based Remote Sensing of the Mixing-layer
23 Height – a Review, *Meteorologische Zeitschrift*, 17, 621-630, 2008.

24 Guo, P., Kuo, Y.-H., Sokolovskiy, S. V., and Lenschow, D. H.: Estimating Atmospheric
25 Boundary Layer Depth using COSMIC Radio Occultation Data, *J. Atmos. Sci.*, 68(8), 1703–
26 1713, 2011.

27 Jason, L.: README document for AIRS Level-2 version 005 standard products. Goddard
28 Earth Sciences Data And Information Services Center (Ed., National Aeronautics and Space
29 Administration (NASA), 2008.

1 Jiang, Q. and Wang, S.: Impact of gravity waves on marine stratocumulus variability, J.
2 Atmos. Sci., 69(12), 3633-3651, 2012.

3 Jones, C. R., Bretherton, C. S., and Leon, D.: Coupled vs. decoupled boundary layers in
4 VOCALS-REx, Atmos. Chem. Phys., 11, 7143-7153, 2011.

5 Jordan, N. S., Hoff, R. M., and Bacmeister, J. T.: Validation of Goddard Earth Observing
6 System-version 5 MERRA planetary boundary layer heights using CALIPSO, J. Geophys.
7 Res., 115(D24), D24218, 2010.

8 Kawanishi, T., Sezai, T., Ito, Y., Imaoka, K., Takeshima, T., Ishido, Y., Shibata, A., Miura,
9 M., Inahata, H., and Spencer, R. W.: The Advanced Microwave Scanning Radiometer for the
10 Earth Observing System (AMSR-E), NASDA's contribution to the EOS for global energy and
11 water cycle studies, IEEE Trans. Geosci. Remote Sensing, 41, 184-194, 2003.

12 Klein, S. A. and Hartmann, D. L.: The seasonal cycle of low stratiform clouds, J. Climate, 6,
13 1587-1606, 1993

14 Kong, W., and Fan Y.: Convective boundary layer evolution from lidar backscatter and its
15 relationship with surface aerosol concentration at a location of a central China megacity,
16 Journal of Geophysical Research: Atmospheres, 120 (15), 7928-7940, 2015.

17 Lambrightsen, B. H. and Lee, S.-Y.: Coalignment and synchronization of the AIRS instrument
18 suite, IEEE T. Geosci. Remote, 41, 343-351, 2003.

19 Leon, D. C., Wang, Z. and Liu, D.: Climatology of drizzle in marine boundary layer clouds
20 based on 1 year of data from CloudSat and Cloud-Aerosol Lidar and Infrared Pathfinder
21 Satellite Observations (CALIPSO), J. Geophys. Res., 113, D00A14, 2008.

22 Leventidou, E., Zanis, P., Balis, D., Giannakaki, E., Pytharoulis, I., and Amiridis, V.: Factors
23 affecting the comparisons of planetary boundary layer height retrievals from CALIPSO,
24 ECMWF and radiosondes over Thessaloniki, Greece, Atmospheric Environment, 74, 360-
25 366, 2013.

26 Lewis, E. R., and Coauthors, 2012: MAGIC: Marine ARM GPCI Investigation of Clouds.
27 DOE/SC-ARM-12-020, U.S. Department of Energy, 12 pp.

28 Luo, T., Yuan, R. M. and Wang, Z.: Lidar-based remote sensing of atmospheric boundary
29 layer height over land and ocean, Atmos. Meas. Tech., 7, 1-10, 2014a.

1 Luo, T., Yuan, R. M., and Wang, Z.: On factors controlling marine boundary layer aerosol
2 optical depth, *Journal of Geophysical Research: Atmospheres*, 119(6), 3321-3334, 2014b.

3 Luo, T., Yuan, R. M., Wang, Z. and Zhang, Z.: Quantifying the Hygroscopic Growth of
4 Marine Boundary Layer Aerosols by Satellite-Based and Buoy Observations. *J. Atmos.*
5 *Sci.*, **72**, 1063-1074, 2015.

6 McGrath-Spangler, E. L., and Denning A. S.: Estimates of North American summertime
7 planetary boundary layer depths derived from space-borne lidar, *J. Geophys. Res.*,
8 117(D15101), 2012.

9 McGrath-Spangler, E. L., and Denning A. S.: Global seasonal variations of midday planetary
10 boundary layer depth from CALIPSO space-borne LIDAR, *J. Geophys. Res. Atmos.*, 118,
11 1226–1233, 2013.

12 Melfi, S. H., Sphinhirne, J. D., Chou, S. H., and Palm, S. P.: Lidar observations of the
13 vertically organized convection in the planetary boundary layer over the ocean, *J. Climate*
14 *Appl. Meteorol.*, 24, 806-821, 1985.

15 Minnis, P., Heck, P. W., Young, D. F., Fairall, C. W., and Snider, J. B.: Stratocumulus cloud
16 properties derived from simultaneous satellite and island-based instrumentation during FIRE,
17 *J. Appl. Meteorol.*, 31, 317-339, 1992.

18 Norris, J. R., Leovy, C. B.: Interannual variability in stratiform cloudiness and sea surface
19 temperature, *J. Climate*, 7, 1915-1925, 1994.

20 Norris, J. R.: Low cloud type over the ocean from surface observations. Part I: relationship to
21 surface meteorology and the vertical distribution of temperature and moisture, *J. Climate*, 11,
22 369-382, 1998.

23 Overoye, K., Aumann, H. H., Weiler, M. H., Gigioli, G. W., Shaw, W., Frost, E., and McKay,
24 T.: Test and calibration of the AIRS instrument, *SPIE Proceedings*, 3759, 254-265, 1999.

25 Pagano, T. S., Aumann, H. H., Hagan, D. E. and Overoye, K.: Prelaunch and in-flight
26 radiometric calibration of the Atmospheric Infrared Sounder (AIRS), *IEEE Trans. Geosci.*
27 *Remote Sens.*, 41, 265–273, 2003.

28 Palm, S. P., Benedetti, A., and Sphinhirne, J.: Validation of ECMWF global forecast model
29 parameters using GLAS atmospheric channel measurements, *Geophys. Res. Lett.*, 32(22),
30 L22S09, 2005.

1 Partain P.: Cloudsat ECMWF-AUX auxiliary data process description and interface control
2 document, 2004.

3 Piironen, P., and Eloranta, E. W.: Demonstration of a high spectral resolution lidar based on
4 an iodine absorption filter, Optics letters, 19, 234-236, 1994.

5 Ratnam, M. V. and Basha, S. G.: A Robust Method to Determine Global Distribution of
6 Atmospheric Boundary Layer Top from COSMIC GPS RO Measurements, Atmos. Sci. Let,
7 11, 216–222, 2010.

8 Randall, D. A., Abeles, J. A. and Corsetti, T. G.: Seasonal simulations of the planetary
9 boundary layer and boundary-layer stratocumulus clouds with a general circulation model. J.
10 Atmos. Sci., 42, 641-675, 1985.

11 Randall, D. A., Shao, Q., and Branson M. : Representation of clear and cloudy boundary
12 layers in climate models, in Clear and Cloudy Boundary Layers, edited by A. A. M. Holtslag,
13 and P. G. Duynkerke, pp. 305–322, Royal Netherlands Academy of Arts and Sciences,
14 Amsterdam, 1998.

15 Randall, D.A., Wood, R.A., Bony, S., Colman, R., Fichefet, T., Fyfe, J., Kattsov, V., Pitman,
16 A., Shukla, J., Srinivasan, J., Stouffer, R. J., Sumi, A. and Taylor, K.E.: Climate Models and
17 Their Evaluation. In: Climate Change 2007: The Physical Science Basis. Contribution of
18 Working Group I to the Fourth Assessment Report of the Intergovernmental Panel on Climate
19 Change [Solomon, S., D. Qin, M. Manning, Z. Chen, M. Marquis, K.B. Averyt, M.Tignor and
20 H.L. Miller (eds.)]. Cambridge University Press, Cambridge, United Kingdom and New York,
21 NY, USA, 2007.

22 Sassen, K. and Z. Wang, 2012: The Clouds of the Middle Troposphere: Composition,
23 Radiative Impact, and Global Distribution, Surv. Geophys., 3, 677-691, 2012.

24 Seidel, D. J., Ao, C. O., and Li K.: Estimating climatological planetary boundary layer heights
25 from radiosonde observations: comparison of methods and uncertainty analysis, J. Geophys.
26 Res., 115, D16113, 2010.

27 Shipley, S. T., Tracy D. H., Eloranta, E. W., Trauger, J. T., Sroga, J. T., Roesler, F. L. and
28 Weinman, J. A.: A High Spectral Resolution Lidar to measure optical scattering properties of
29 atmospheric aerosols, Part I: Instrumentation and theory, Applied Optics, 23, 3716-3724, 1983.

1 Stephens, G. L., Vane, D. G., Boain, R. J., Mace, G. G., Sassen, K., Wang, Z., Illingworth, A.,
2 J., O'Connor, E. J., Rossow, W. B., Durden, S. L., Miller, S. D., Austin, R. T., Benedetti, A.,
3 Mitrescu, C., and The CloudSat Science Team: THE CLOUDSAT MISSION AND THE A-
4 TRAIN. *Bull. Amer. Meteor. Soc.*, 83, 1771-1790, 2002.

5 Stull, R. B. and Eloranta, E. W.: Boundary Layer Experiment 1983, *Bull. Amer. Meteorol.*
6 *Soc.*, 65, 450–456, 1984.

7 Susskind, J., Barnet, C., Blaisdell, J., Iredell, L., Keita, F., Kouvaris, L., Molnar, G., and
8 Chahine, M.: Accuracy of geophysical parameters derived from Atmospheric Infrared
9 Sounder/Advanced Microwave Sounding Unit as a function of fractional cloud cover, *J.*
10 *Geophys. Res.*, 111, D09S17, 2006.

11 Tanelli, S., Durden, S. L., Im, E., Pak, K. S., Reinke, D. G., Partain, P., Haynes, J. M., and
12 Marchand, R. T.: CloudSat's cloud profiling radar after two years in orbit: Performance,
13 calibration, and processing. *Geoscience and Remote Sensing, IEEE Transactions on*, 46(11),
14 3560-3573, 2008.

15 Vanzanten, M. C., Duynkerke, P. G., and Cuijpers, J. W.: Entrainment parameterization in
16 convective boundary layers, *J. atmos. sci.*, 56(6), 813-828, 1999.

17 Vogelzang, D., and Holtslag, A.: Evaluation and model impacts of alternative boundary-layer
18 height formulations. *Bound.-Layer Meteor.*, 81, 245-269, 1996.

19 Wang, Z., D. Vane, G. Stephens, and D. Reinke, 2012: Level 2 combined radar and lidar
20 cloud scenario classification product process description and interface control document. JPL
21 Rep., 22 pp. Available online at
22 <http://www.cloudsat.cira.colostate.edu/sites/default/files/products/files/2B-CLDCLASS->
23 LIDAR_PDICD.P_R04.20120522.pdf [Accessed 2016/02/25].

24 Wentz, F. J., Gentemann C. and Ashcroft, P.: On-orbit calibration of AMSR-E and the
25 retrieval of ocean products, 83rd AMS Annual Meeting, American Meteorological Society,
26 Long Beach, CA, 2003.

27 Wentz, F.J., T. Meissner, C. Gentemann, and M. Brewer: Remote Sensing Systems AQUA
28 AMSR-E Daily Environmental Suite on 0.25 deg grid, Version 7.0. Remote Sensing
29 Systems, Santa Rosa, CA, 2014. Available online at www.remss.com/missions/amsre
30 [Accessed 2016/02/25].

1 Winker, D. M., Hunt, W. H., and McGill M. J.: Initial performance assessment of CALIOP,
2 Geophys. Res. Lett., 34(19), L19803, 2007.

3 Winker, D. M., Vaughan, M. A., Omar, A., Hu, Y., Powell, K. A., Liu, Z., Hunt, W. H., and
4 Young, S. A.: Overview of the CALIPSO mission and CALIOP data processing algorithms, J.
5 Atmos. Oceanic Technol., (26), 2310-2323, 2009.

6 Wood R. and Bretherton C. S.: Boundary layer depth, entrainment, and decoupling in the
7 cloud-capped subtropical and tropical marine boundary layer, J. Climate, 17, 3576-3588,
8 2004.

9 Wood, R., and Bretherton, C. S.: On the relationship between stratiform low cloud cover and
10 lower-tropospheric stability, J. Climate, 19(24), 6425–32, 2006.

11 Wyant, M. C., Wood, R., Bretherton, C. S., Mechoso, C. R., Bacmeister, J., Balmaseda, M.
12 A., Barrett, B., Codron, F., Earnshaw, P., Fast, J., Hannay, C., Kaiser, J. W., Kitagawa, H.,
13 Klein, S. A., Köhler, M., Manganelli, J., Pan, H.-L., Sun, F., Wang, S., and Wang, Y.: The
14 PreVOCA experiment: modeling the lower troposphere in the southeast Pacific, Atmos.
15 Chem. Phys., 10, 4757-4774, 2010.

16 Wyant, M. C., Bretherton, C. S., Wood, R., Carmichael, G. R., Clarke, A., Fast, J.,
17 George, R., Gustafson Jr., W. I., Hannay, C., Lauer, A., Lin, Y., Morcrette, J.-J., Mulcahy, J.,
18 Saide, P. E., Spak, S. N., and Yang, Q.: Global and regional modeling of clouds and aerosols
19 in the marine boundary layer during VOCALS: the VOCA intercomparison, Atmos. Chem.
20 Phys., 15, 153-172, 2015.

21 Xie, F., Wu, D. L., Ao, C. O., Mannucci, A. J., and Kursinski, E. R.: Advances and
22 Limitations of Atmospheric Boundary Layer Observations with GPS Occultation over
23 Southeast Pacific Ocean, Atmos. Chem. Phys., 12, 903-918, 2012.

24 Yue, Q., Kahn, B. H., Fetzer, E. J., and Teixeira, J.: Relationship between marine boundary
25 layer clouds and lower tropospheric stability observed by AIRS, CloudSat, and CALIOP, J.
26 Geophys. Res., 116, D18212, 2011.

27 Zhou, X., Kollias, P., and Lewis, E. R.: Clouds, precipitation, and marine boundary layer
28 structure during the magic field campaign. J. Climate, 28, 2420–2442, 2015.

1 Zhang, C., Wang, Y., Hamilton, K.: Improved representation of boundary layer clouds over
2 the southeast Pacific in ARW-WRF using a modified tiedtke cumulus parameterization
3 scheme, *Mon. Wea. Rev.*, 139, 3489-3513, 2011.

4 Zhou, X., Kollias, P., and Lewis, E. R.: Clouds, precipitation and marine boundary layer
5 structure during the MAGIC field campaign, *Journal of Climate*, 28, 2420-2442, 2015.

6 Zuidema, P., Painemal, D., Szoek, S. de, Fairall, C.: Stratocumulus cloud-top height
7 estimates and their climatic implications, *J. Climate*, 22, 4652-4666, 2009.

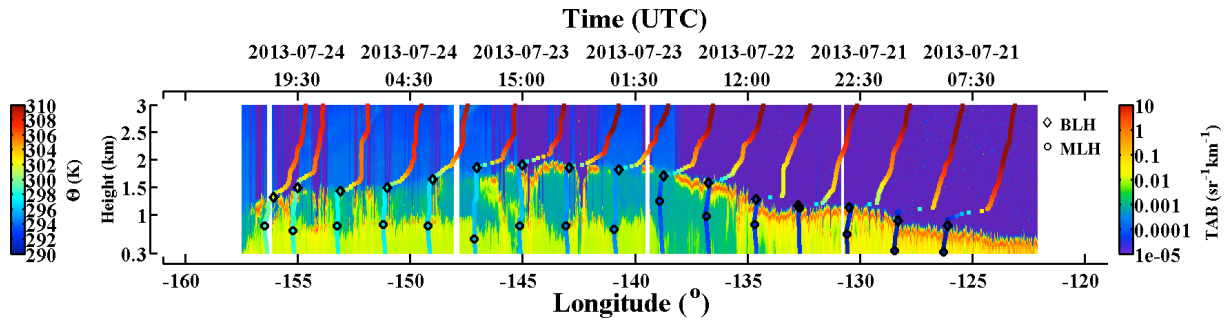
8

9

10

11

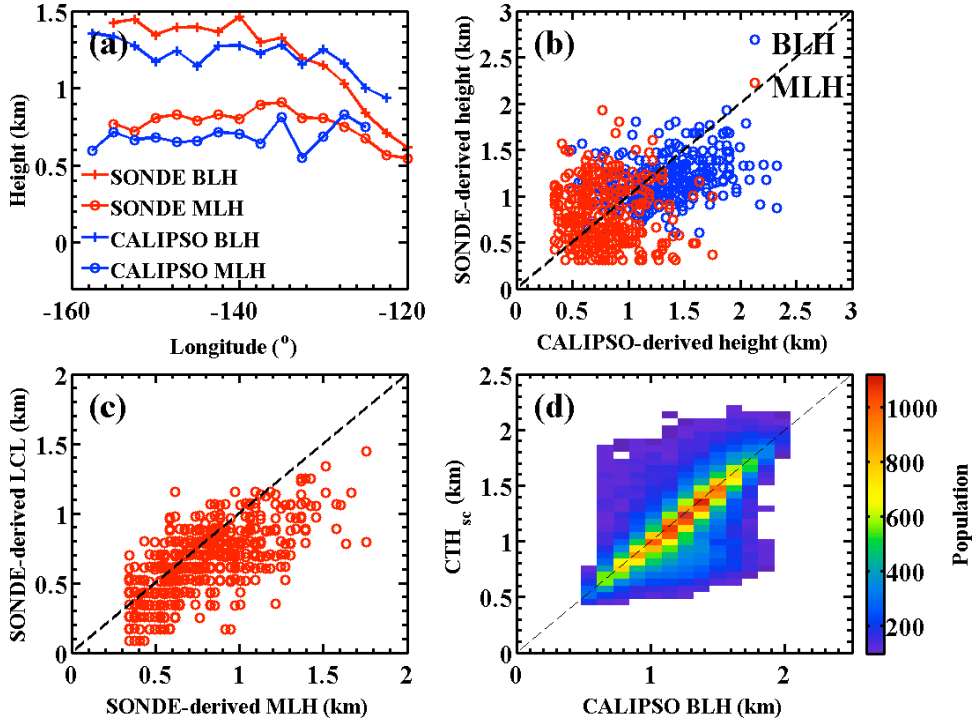
1



2

3

4 Figure 1. Potential temperature profiles and retrieved MBL structure (black diamonds for
 5 BLH and black circles for MLH) for a MAGIC leg from 2013/07/21 - 2013/07/24, overlaid
 6 with total attenuated backscattering from HSRL.



7

8

9 Figure 2. (a) Mean MBL structure along longitude from MAGIC radiosonde and collocated
 10 CALIOP observations; (b) comparisons of radiosonde and CALIOP derived BLH and MLH;
 11 (c) comparison of radiosonde derived MLH and LCL; (d) comparison of CALIOP derived
 12 BLH and stratiform cloud top (CTH_{sc}).

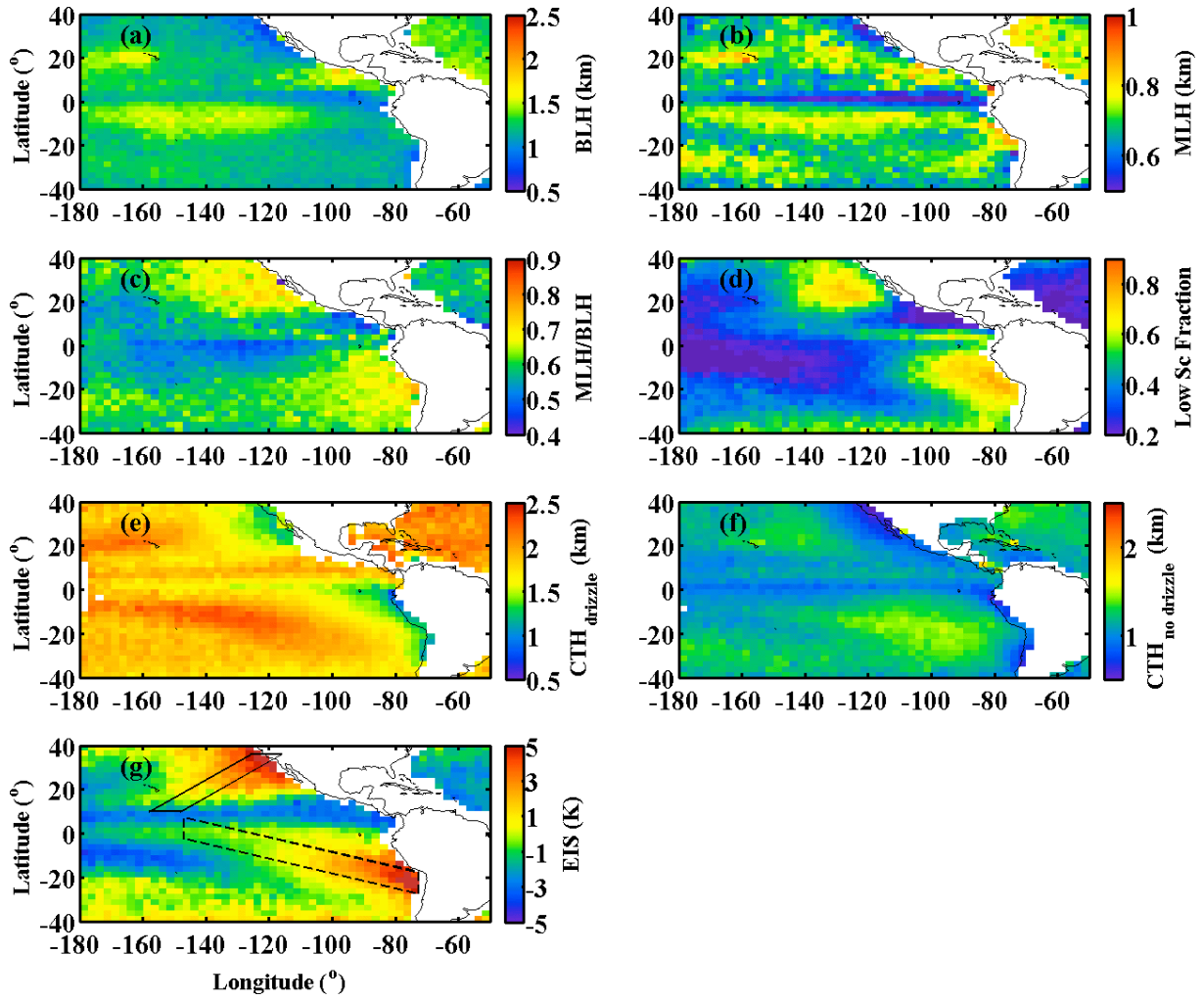
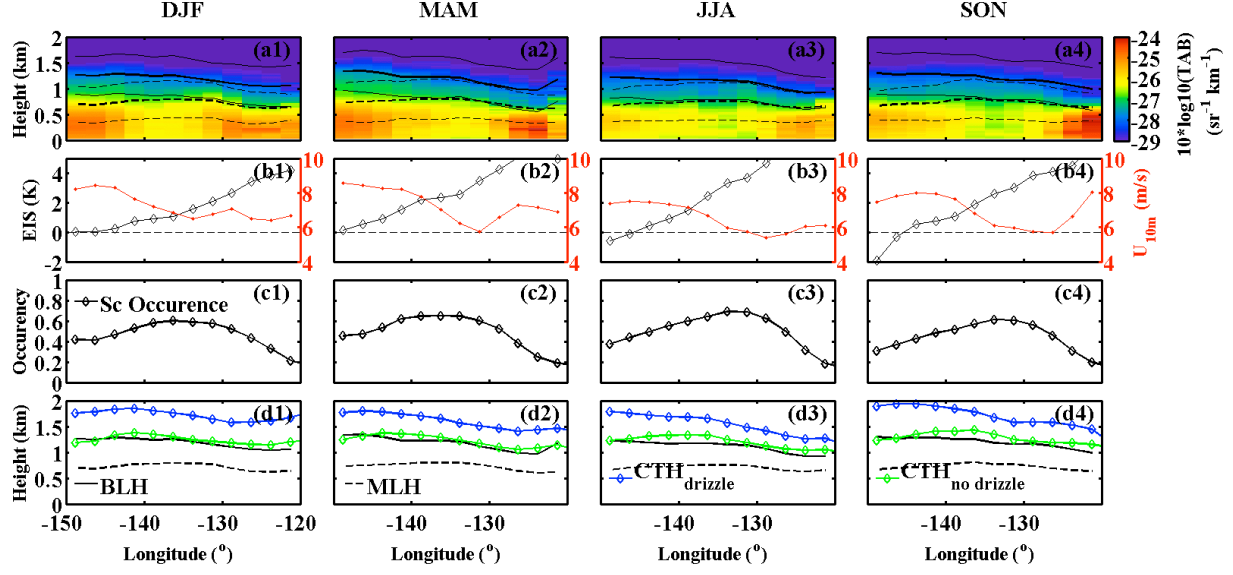
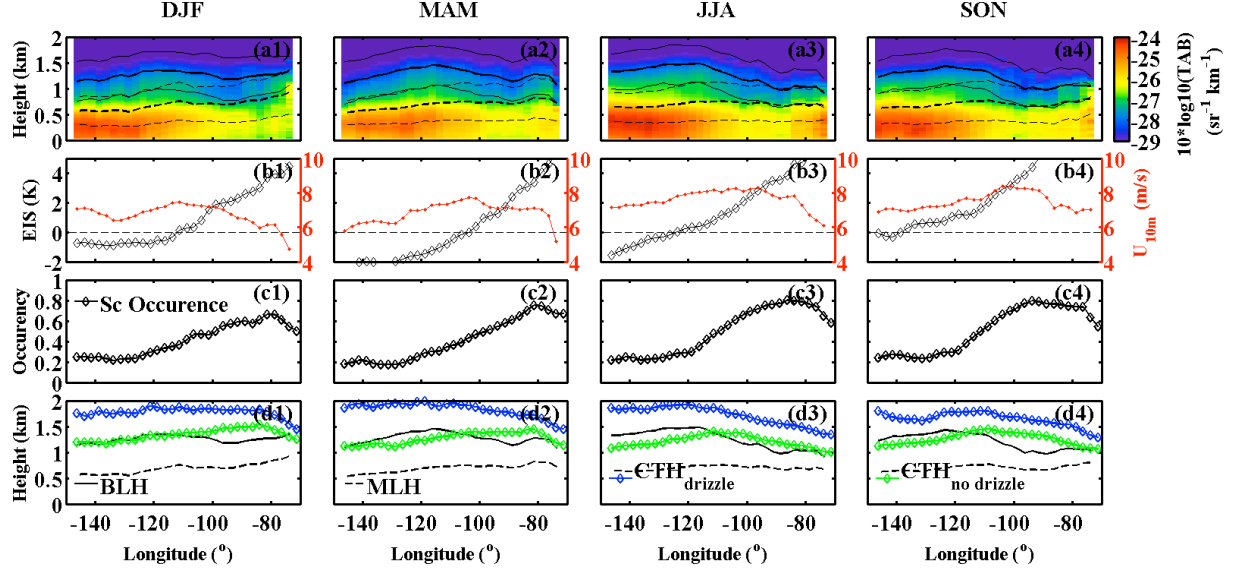


Figure 3. The spatial distribution of (a) CALIOP derived BLH, (b) CALIOP derived MLH, (c) CALIOP derived MBL decoupling structure in term of MLH/BLH, (d) Marine low clouds fraction, (e) drizzled stratiform CTH ($CTH_{drizzle}$), (f) non-drizzled stratiform CTH ($CTH_{no_drizzle}$), (g) EIS. The solid and dashed boxes in (g) denote the selected transects on the northeastern and southeastern Pacific Ocean (NPO and SPO) used in Figs. 4 and 5 respectively.



1 Figure 4: The satellite MBL observations along the transect region on the northeastern Pacific
 2 Ocean (NPO, solid box in fig 3e) in different seasons: (a1-a4) the mean BLH (solid line) and
 3 MLH (dashed line) overlaid with TAB, and corresponding standard deviations (thin solid and
 4 dashed lines); (b1-b4) EIS (black diamond line) and U_{10m} (red dot line); (c1-c4) stratocumulus
 5 (Sc) occurrence; (d1-d4) comparisons of BLH, MLH, $CTH_{drizzle}$, and $CTH_{no\ drizzle}$.



9 Figure 5: Same as Fig. 4 but for the transect region on the southeastern Pacific Ocean (SPO,
 10 dashed box in fig 3e) in different seasons.

11

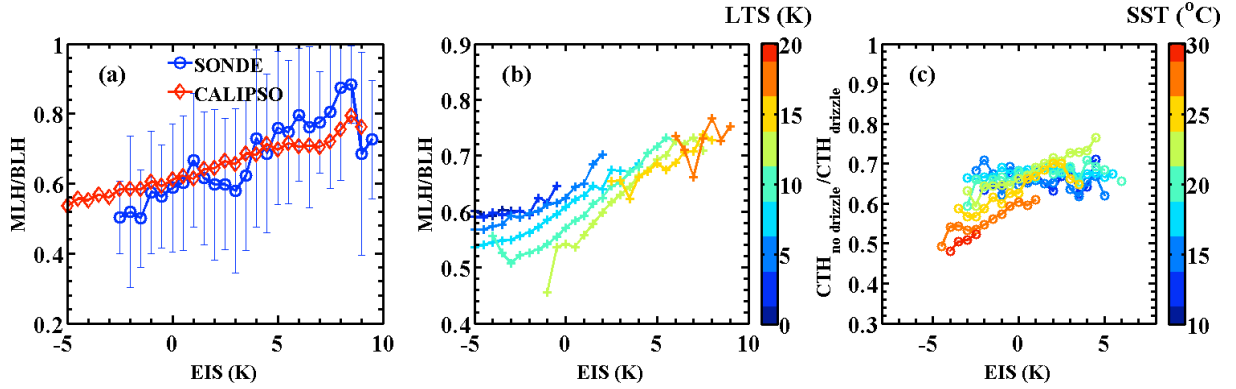


Figure 6. (a) Relationship with EIS and MLH/BLH in MAGIC and Satellite observations over extended MAGIC region; (b) relationship between EIS and CALIOP-derived MLH/BLH under different LTS over the global oceans; (c) seasonal mean relationship between EIS with CTH_{no drizzle}/CTH_{drizzle} under different SST over the global oceans. The standard deviations in the figures (a) and (b) are ~ 0.2 , and ~ 0.1 in (c).

7

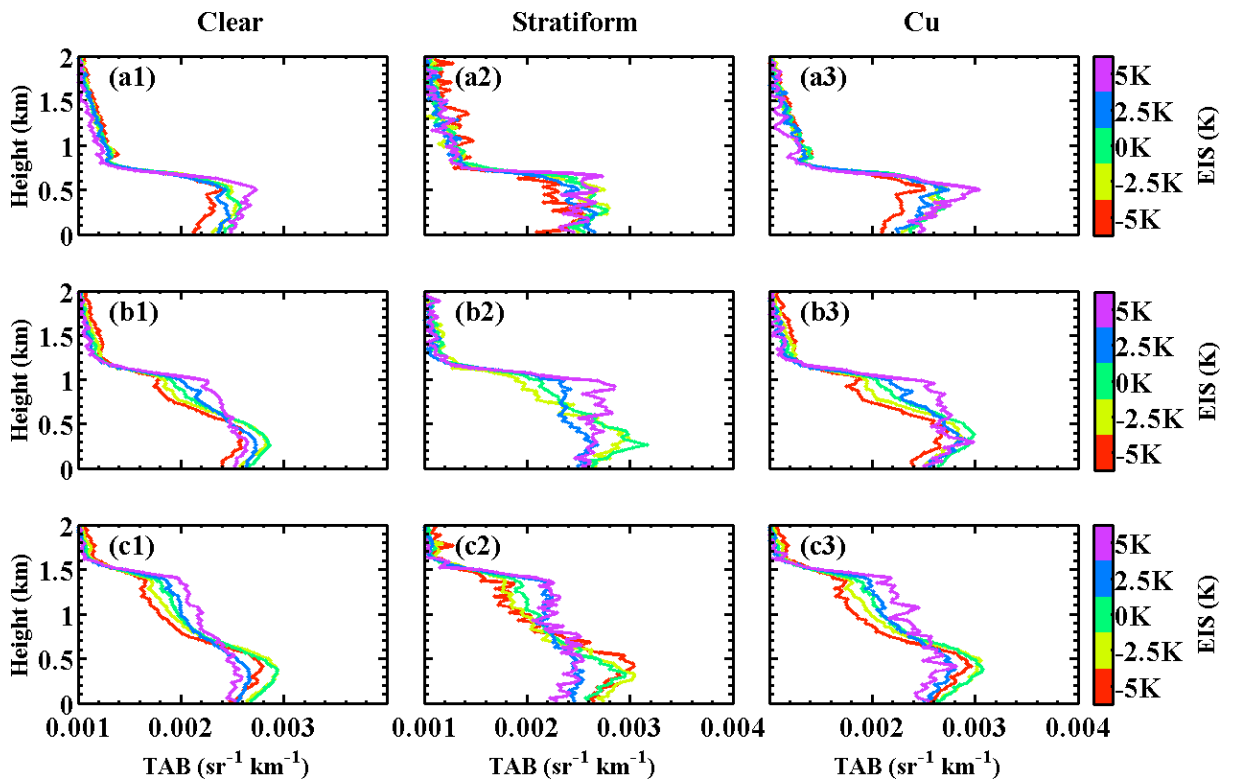


Figure 7. Mean MBL CALIOP TAB structure under different conditions from 4-year climatology over the eastern Pacific Ocean: $0.6\text{ km} < \text{BLH} < 0.8\text{ km}$ (a1, a2, a3), $1\text{ km} < \text{BLH} < 1.2\text{ km}$ (b1, b2, b3), and $1.4\text{ km} < \text{BLH} < 1.6\text{ km}$ (c1, c2, c3). (a1, b1, c1) are under the clear conditions that is defined as totally cloud-free over a 0.25° AMSR-E footprint; (a2, b2, c2) are under the stratiform cloud conditions that is defined as with only stratiform cloud and

1 clear sky in each 0.25° AMSR-E footprint; (a3, b3, c3) are under the Cu cloud conditions that
2 is defined as with only Cu cloud and clear sky in each 0.25° AMSR-E footprint. Only results
3 with $5 \text{ m/s} < U_{10\text{m}} < 8 \text{ m/s}$ were included.